Journal of Porous Materials (2023) 30:619–628
https://doi.org/10.1007/s10934-022-01367-2

Enhanced antimicrobial activity of volatile thymol molecules encapsulated in hierarchical titanosilicates

Melda Isler Binay[1] · Didem Kart[2] · Burcu Akata[1,3]

Accepted: 8 October 2022 / Published online: 28 October 2022
© The Author(s), under exclusive licence to Springer Science+Business Media, LLC, part of Springer Nature 2022

Abstract
Realizing higher loading and extended-release time of bulkier molecules for enhanced antibacterial activity can be a challenge, which is highly dependent on the pore characteristics of the network used for their encapsulation. This study highlights that the hierarchical microporous Engelhard titanosilicate ETS-10 crystals support a higher amount of thymol encapsulation to allow long-term thymol release and higher antimicrobial activity. In this study, post-synthesis treatment of ETS-10 was performed with H_2O_2 at two different concentrations to induce hierarchical porosity resulting in a gradual increase in surface area and pore volume of ETS-10. The thymol encapsulated and post-treated ETS-10 crystals with enlarged porosity were shown to exhibit enhanced antimicrobial activity against *P. aeruginosa, S. aureus, and C. albicans* compared to untreated ones. Furthermore, the thymol release time was prolonged significantly in addition to an altered release profile. Our findings suggest that tailoring pore characteristics by a simple post-treatment applied to microporous networks creating some hierarchical structure can be an alternative approach for enhanced antimicrobial activity and prolonged release of oil extracts that are vulnerable to environmental conditions.

Keywords Thymol · Hierarchical titanosilicates · Antimicrobial activity · Controlled release · Kinetics

1 Introduction

Essential oil (EO) extracts of plants have been used as alternatives to hazardous synthetic antimicrobial agents due to their remarkable antimicrobial, antiviral, and antioxidant activity [1–4]. Essential oils (EOs) commonly consist of aromatic compounds that influence antibacterial activities, such as terpenes and terpenoids, which are known to disturb the plasma membrane leading to cell death [2, 5, 6]. The antibacterial activity obtained using EOs is generally attributed to the different chemical compounds and varying chemical profiles that show selective antibacterial activity against pathogenic bacteria [7]. Thymol (2-isopropyl-5-methylphenol) is a lipophilic terpene, and it is the main component of thyme *(Thymus vulgaris)* and oregano *(Organum vulgare)*, which can accommodate itself to the membrane's polar-head group region resulting in an increased extracellular ATP and disruption of the cytoplasmic membrane [8, 9]. Thymol has been used for its potential benefits in biomedical applications due to its antibacterial and antioxidant properties [10, 11]. It exhibits biocide activity against gram-negative and gram-positive bacteria such as *Pseudomonas aeruginosa*, *Staphylococcus aureus, Bacillus subtilis*, and *Enterobacter aerogenes* strains [8, 12–15]. Also, it is known that the biocide activity of thymol against *Aspergillus flavus* as fungi and *Candida albicans* as yeast [8, 13, 14].

The main drawbacks of utilizing EOs as an antimicrobial agent are its inherent volatility and tendency to oxidize [16]. Encapsulating EOs in porous structures, such as chitosan [17], cyclodextrin [18–20], starch [21], permutate [22], and cellulose acetate fibrous matrix [23, 24] can be an alternative approach to overcome these limitations. This process offers high efficiency with a controlled release of the loaded compound owing to its protection from the surrounding environment providing physical and chemical stability [25]. Accordingly, many studies based on silica as a host material have been developed to encapsulate such molecules due to

✉ Melda Isler Binay
meldasler@gmail.com

[1] Micro and Nanotechnology Programme, Middle East Technical University, 06800 Ankara, Turkey

[2] Faculty of Pharmacy, Hacettepe University, 06100 Ankara, Turkey

[3] Central Laboratory, Middle East Technical University, 06800 Ankara, Turkey

their high surface area and adjustable particle size [2, 12, 25–27]. In these studies, surface modification of mesoporous silica was required to ensure the adsorption of EOs [2, 26] and antioxidants [28] with controlled release. However, the initial burst release of encapsulated compounds from larger pores can be problematic, resulting in low therapeutic efficiency. The release profile in mesoporous compounds can be tailored by utilizing different surfactants and functionalizing agents [2, 27]. Nevertheless, these processes narrow down the pore size of the host material, reducing the amount loaded into the pores and eliminating the benefit of using a mesoporous host to encapsulate the guest molecules.

The generation of intra-crystalline mesopores can be an alternative strategy to tailor the adsorption and release profile of EOs. Herein, a new approach was proposed by creating such hierarchical porosity to encapsulate thymol molecules eliminating the need to use surfactants and functionalizing agents. For that purpose, the pore size of microporous titanosilicate ETS-10 crystals was enlarged through post-synthesis modifications with hydrogen peroxide treatment [29]. The role of induced enlargement in ETS-10 porosity on thymol loading and its effect on the thymol release profiles were investigated. The finely tuned samples using ETS-10 treated with aqueous H_2O_2 solution for two different time intervals were further investigated for their antibacterial activities, making them excellent candidates as novel hosts for natural antibacterial components extracted from plants.

2 Materials and methods

The chemicals; TiO_2 (Degussa P25, 76 wt% anatase, and 24 wt% rutile) and $NaSiO_2$ were obtained from Sigma-Aldrich. NaCl (99.0%), KCl (99.0%), and H_2SO_4 (96.5%) were received from JT Baker for the synthesis of ETS-10. H_2O_2 (50 wt% in H_2O), thymol (≥ 98.5%), NaOH, and HCl were purchased from Sigma-Aldrich. Phosphate buffer saline (PBS) was purchased from Chem-Lab. Deionized water is distilled from running tap water with a water purification system (Milli-Q system). All glassware was cleaned with deionized water and dried in an oven at 373 K. Materials for antimicrobial analyses were as follows. Mueller–Hinton and Saburaud dextrose agar (SDA) were purchased from Merck. Ciprofloxacin (≥ 98%) and fluconazole (≥ 98%) were obtained from Sigma-Aldrich. Blank sterile discs were purchased from Sigma-Aldrich for antimicrobial analysis.

2.1 Synthesis and post-Synthesis treatment of ETS-10 crystals

A schematic illustration of the encapsulation of thymol in hierarchical ETS-10 crystals is represented in Fig. 1. ETS-10 crystals were synthesized using a gel with the composition: 3.4 Na_2O: 1.5 K_2O: TiO_2: 5.5 SiO_2: 150 H_2O [30] (Fig. 1a). The Si precursor solution was prepared by dissolving 3.2 g of sodium chloride and 4.9 g of potassium chloride in 28.0 g

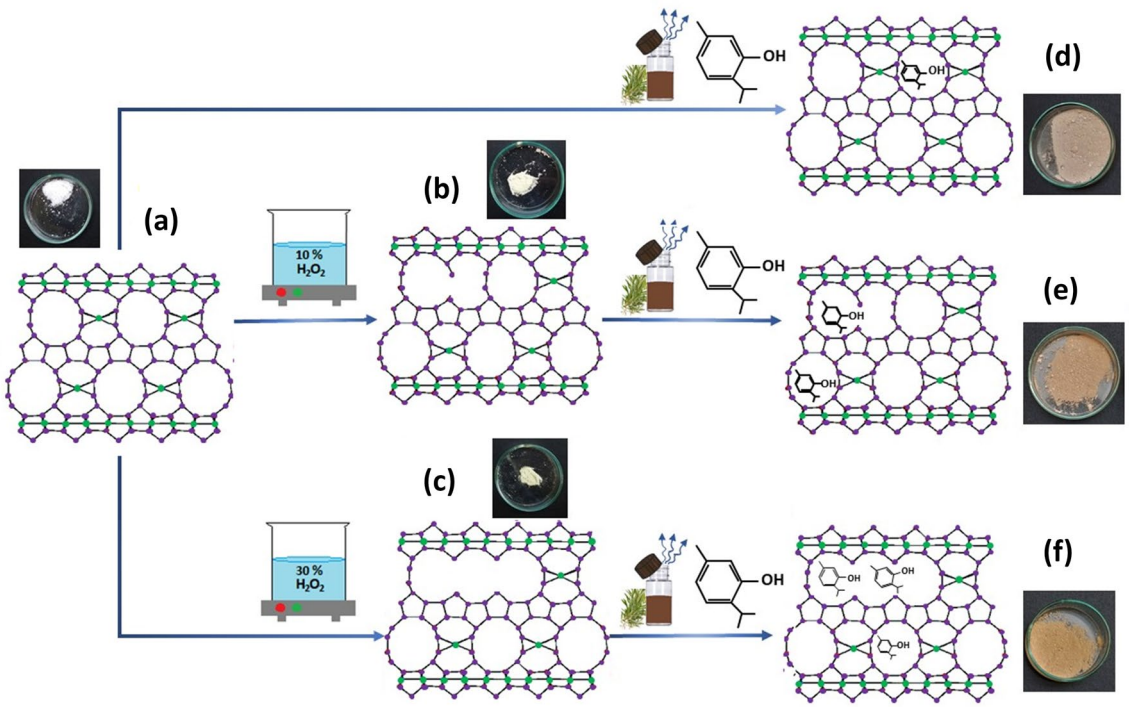


Fig. 1 Schematic illustration of the encapsulation of thymol in hierarchical ETS-10 crystals

of deionized water. After dissolving, 27.6 g of sodium silicate was added to the prepared aqueous salt solution in a high-density polyethylene bottle (HDPE) and hand-shaken for 5 min. For the Ti precursor solution, an aqueous solution of sulfuric acid was prepared with 1.5 g of sulfuric acid and 14.4 g of deionized water, and then 1.8 g of P25 was added to this prepared aqueous sulfuric acid solution. Afterward, the Ti solution was poured into the Si solution. The resulting white, viscous solution was hand-shaken for 8 min. The gel was introduced into 10 mL Teflon-lined stainless-steel autoclaves for 72 h at 503 K. The obtained crystals were cooled to room temperature, centrifuged, and washed with deionized water several times. Finally, the as-synthesized ETS-10 crystals were dried overnight in a conventional oven at 373 K.

The formation of hierarchical ETS-10 samples (10-ETS and 30-ETS) is depicted in Fig. 1b–c. For this purpose, the post-synthesis treatment was performed by subjecting 1 g of as-synthesized ETS-10 crystals (ETS) to 100 mL of 10–30 wt% aqueous H_2O_2 solution for 10 (10-ETS) and 30 min (30-ETS) respectively at room temperature [29]. The treated crystals were washed, centrifuged three times with deionized water, and dried overnight in an oven at 323 K.

2.2 Thymol loading

0.5 g of as-synthesized and post-treated ETS-10 crystals and 1 g of thymol were transferred into each separate glass petri dishes. These petri dishes were placed in a closed glass vessel for adsorption for two weeks. This method allowed one to treat a high amount of sample at once under room conditions. The percent encapsulation of each sample was calculated from Eq. (1) [31];

$$\%Encapsulation = \frac{weight\ of\ thymol\ \left(m_{THY}\right)}{weight\ of\ zeolite\ \left(m_{ETS}\right)} \times 100 \quad (1)$$

where m_{ETS} is the initial weight of ETS-10 and m_{THY} is the weight difference of ETS-10 crystals before and after placing them in the desiccator. The thymol-loaded samples were denoted as ETS-thy, 10-ETS-thy, and 30-ETS-thy for ETS, 10-ETS, and 30-ETS, respectively (Fig. 1d–f).

2.3 Release assay and kinetics

The release assays of thymol were studied using UV-Vis spectrophotometer at 274 nm. In a typical release assay, 25 mg of thymol-loaded ETS-10 crystals were immersed in 20 mL of PBS without stirring. After a predetermined interval, 2 mL of a solution suspension was taken off, measured, and then put back into the suspension. The release assays were examined for ten days. The released concentration of thymol was determined via the acquired calibration curve of thymol at 274 nm (Supplementary Information Fig. S1). To further study thymol release mechanisms from the hierarchical structures, various kinetic models were conducted to determine the release mechanism equations, such as Higuchi [31], Korsmeyer-Peppas [23, 32], Elovich [25], and Hixson-Crowell [33]. The percentage of cumulative thymol release was calculated based on Eq. (2).

$$\%cumulative\ thymol\ release = \sum \frac{M_t}{M_0} \times 100 \quad (2)$$

2.4 Antimicrobial assays

The antimicrobial activities of ETS-thy, 10-ETS-thy, and 30-ETS-thy on *P. aeruginosa* (ATCC 27,853), *S. aureus* (ATCC 29,213), and *C. albicans* (90,028) were determined by the disc diffusion method. The bacteria and *C.albicans* yeast inoculums were suspended in sterile saline, diluted according to 0.5 McFarland standard, and then spread on Mueller–Hinton agar (Merck) and Saburaud dextrose agar (SDA) plates, respectively. The ethanol suspensions of thymol-loaded ETS-10 crystals were prepared (20% wt/wt). All pathogenic organisms were inoculated on Mueller–Hinton agar (Merck) at 37 °C overnight. Paper discs dropped with 140 µL thymol-loaded ETS-10 crystals were located on agar plates. The plates were incubated at 37 °C for 24 h. After incubation, the inhibition zones (mm) were measured. Ciprofloxacin (5 µg) and fluconazole (25 µg) were used as standards. In the presented study, all the antimicrobial experiments were repeated three times (n = 3), and representative data are presented as the mean inhibition zone value of the compounds.

2.5 Characterization

The morphologies of all ETS-10 crystals were observed by field-emission scanning electron microscope (FE-SEM, FEI Quanta 400) and high-resolution transmission electron microscope (HR-TEM, JEOL JEM 2100 F). 0.01 g of ETS-10 in ethanol suspension dropped onto the copper grid, and 200 kV of operating voltage was used for TEM imaging. Phase identification of as-synthesized and post-synthesis treated ETS-10 crystals was performed by X-ray powder diffraction (XRD) using Rigaku-Ultima IV. The diffraction peaks were scanned between 5° and 40° with a 1°/min scan speed. The Raman spectra were measured by a Renishaw type Raman microscope with an excitation wavelength of 532 nm. The Brunauer-Emmett-Teller (BET) method was applied by Quantachrome Corporation, Autosorb-6, to determine the total surface area and pore size distribution. Powder ETS-10 crystals were analyzed by Fourier transform infrared (FTIR) spectroscopy (Thermo Scientific Nicolet

iS10) with attenuated total reflection (ATR) attachment. The spectra were recorded in the 1800 – 600 cm^{-1}. Thymol content was evaluated using a Diffuse reflectance UV–vis spectrophotometer (Agilent Technologies Cary 60). The collected DR-UV-vis spectra were converted to absorption spectra by using Kubelka–Munk function [$(1\text{-}R)^2/2R$], where the diffuse reflection of the sample (R).

3 Results and discussions

3.1 Synthesis of ETS-10 and post-synthesis treatments of ETS-10 crystals

The FE-SEM and HR-TEM images of as-synthesized and hierarchical ETS-10 crystals are shown in Fig. 2. Crystals in all ETS-10 samples maintained the same elongated square-based truncated bipyramidal morphology (Fig. 2a–c). Figure 2d–f depicts the HR-TEM images of as-synthesized and hierarchical ETS-10 crystals taken along the *a* or *b* direction, as stated in the literature [29]. The bright dots identify the large 12-membered ring pores that are typical of the ETS-10 (Fig. 1a). In the TEM micrographs of hierarchical ETS-10 samples, a significant number of larger white dots were detected that were not present in the parent sample, as indicated by the red arrows in Fig. 2e–f. These larger dots were formed by the removal of Ti atoms and the neighboring SiO_4 tetrahedra from the framework after breaking Ti–O–Ti bonds (Fig. 1b–c and e–f) [29].

The X-ray diffraction patterns of as-synthesized and hierarchical ETS-10 crystals present in Fig. 3. The XRD pattern of synthesized parent sample (i.e., ETS) is consistent with the literature [34], and the XRD patterns of 10-ETS and 30-ETS match well with that of parent sample, and no additional peaks were observed (Fig. 3). The relative crystallinity of the treated samples was calculated by comparing the peak area in the range of $2\theta = 24.65 - 27.50$ with that of the parent sample (ETS) [35]. Accordingly, the relative crystallinity of treated

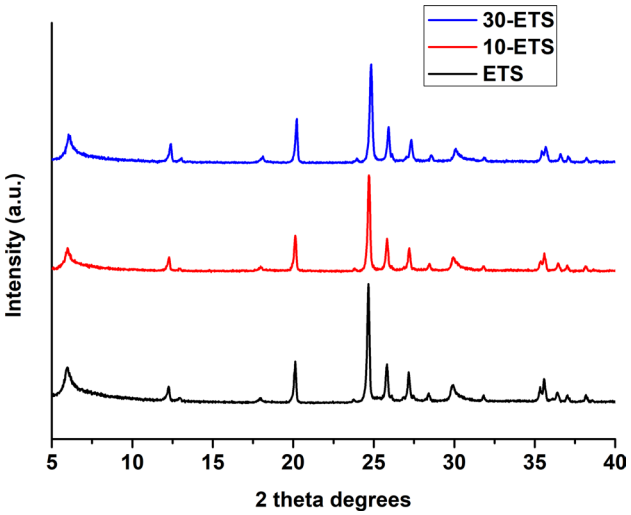


Fig. 3 XRD patterns of ETS, 10-ETS, 30-ETS.

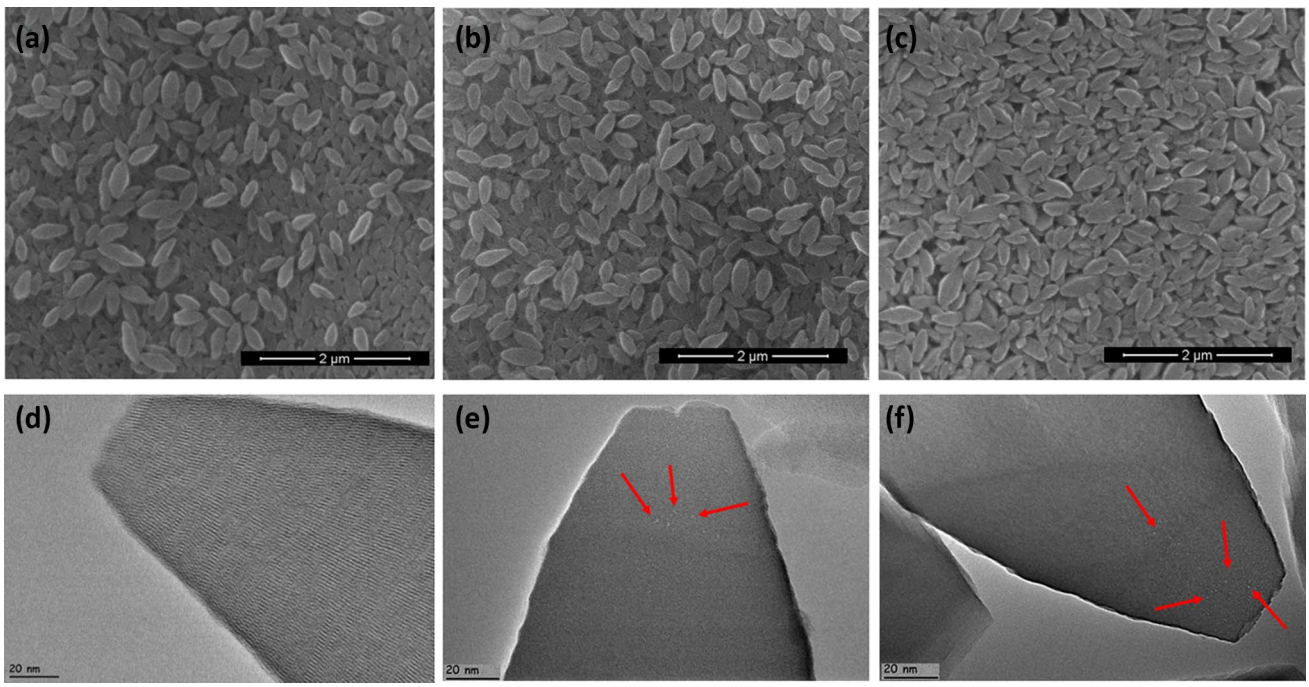


Fig. 2 FE-SEM images of ETS (**a**), 10-ETS (**b**), 30-ETS (**c**), and HR-TEM images of ETS (**d**), 10-ETS (**e**), 30-ETS (**f**)

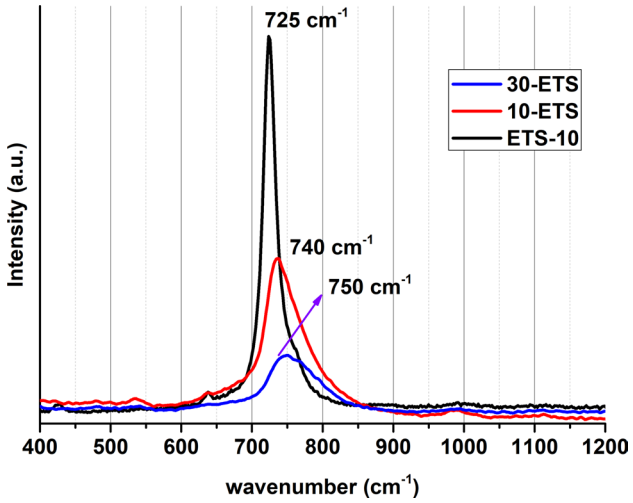


Fig. 4 Raman spectra of ETS, 10-ETS, and 30-ETS.

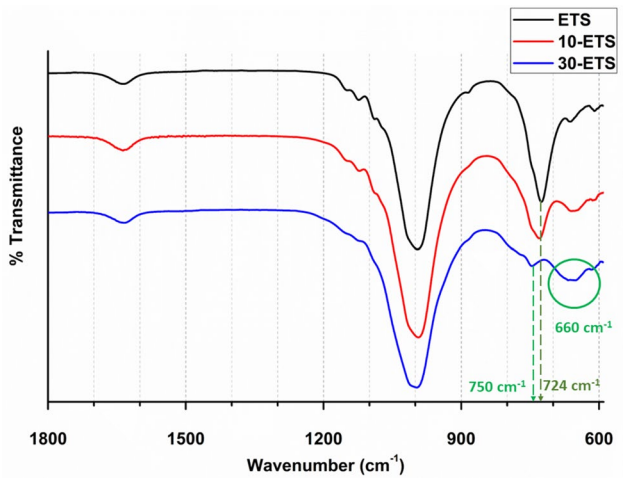


Fig. 5 FTIR spectra of ETS, 10-ETS, and 30-ETS.

10-ETS and 30-ETS samples were 94.9 and 90.6%, respectively, indicating the formation of structural defects in the ETS-10 framework without considerable degradation after post-synthesis treatment.

The Raman spectra of ETS, 10-ETS, and 30-ETS-10 are shown in Fig. 4. The characteristic Ti-O-Ti stretching band of ETS can be seen at 724 cm^{-1}. This band broadened, shifted to higher frequencies, and became less intense upon applying post-synthesis treatment, all known to be related to crystal deterioration [36]. In the current study, the post-synthesis treatments resulted in a progressive broadening and decrease in this band's intensity with induced redshifts of 16 cm^{-1} and 26 cm^{-1} for 10-ETS and 30-ETS, respectively. These changes can be associated with interruptions of Ti–O–Ti chains with induced defects upon increased H_2O_2 concentration.

Figure 5 shows the FTIR spectra of untreated and H_2O_2-treated (10-ETS and 30-ETS) samples. According to Fig. 5, there was no change in the most intense vibrational band originating from the asymmetric Si–O–Si stretching band at 997 cm^{-1} [37]. However, the vibrational band at 724 cm^{-1} originated from the Ti–O–Ti stretching band gradually decreased, followed by a shift to 750 cm^{-1} with the increase in the H_2O_2 concentration, showing the disruption of Ti–O–Ti chains. Moreover, the intensity of the Ti–O–Ti stretching band at 660 cm^{-1} steadily increased with H_2O_2 concentration, associated with the formation of a new Ti complex due to the interaction of H_2O_2. These changes are related to breaking Ti–O–Ti chains through post-synthesis treatment, creating a structure more prone to hierarchical microporosity with defects [29].

3.2 Thymol loading

The UV-vis spectra of ETS, ETS-thy, 10-ETS-thy, and 30-ETS-thy are shown in Fig. 6. The adsorption of H_2O_2 resulted in a change of color into yellow-orange, as shown in Fig. 1 [38]. Thymol is a colorless crystal with maximum absorption at around 274 nm. First, ETS had an upper absorption edge at around 350 nm, which was ascribed to a charge transfer of the O(2p) to Ti(3d) transition [39], as shown in Fig. 6. Upon the interaction of titanosilicate ETS sample with H_2O_2, the intensity of this band progressively increased at higher concentrations of H_2O_2 for 10-ETS and 30-ETS samples, respectively. The adsorption of the thymol molecule on the untreated ETS sample gave rise to a peak around 450 nm. Gradual increase in the concentration of H_2O_2 resulted in a slight blueshift of this band to around 400 nm with increased intensity for 10-ETS-thy and 30-ETS-thy samples.

The reaction of H_2O_2 with titanosilicates containing Ti^{4+} in tetrahedral coordination was investigated in previous studies [29, 38, 40]. The interaction leads to the formation of complexes between peroxy groups and Ti^{4+} [29, 38]. The formed titanium peroxo complexes exhibit new ligand-to-metal charge transfer (LMCT), which was observed at around 400 nm (Fig. 6) [29, 40–42]. The formation of titanium peroxo complexes revealed a change in color from white to yellow. The formed yellow color remained unchanged after washing with double distilled water three times and drying at 323 K (Fig. 1) [43]. In accordance with FTIR results (Fig. 5), the post-synthesis treatment with aqueous H_2O_2 solution triggered breaking Ti-O-Ti chains, forming active Ti sites in the ETS-10 framework [29]. Furthermore, the absorption band above 400 nm suggests a surface complex formation of organic compounds with titania [44]. Accordingly, the loading of thymol into ETS, 10-ETS,

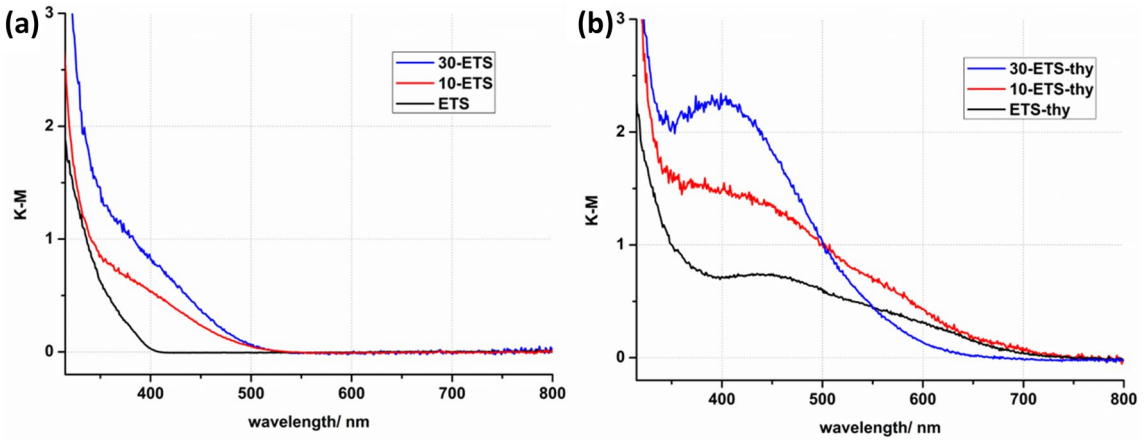


Fig. 6 Diffuse reflectance UV-Vis spectra of ETS-10 samples (**a**) and related thymol loaded ETS-10 samples (**b**)

and 30-ETS gave rise to the formation of an intense peak around 400–450 nm, which was attributed to the formation of new chemical bonds due to the interaction of Ti-O bonds of ETS-10 crystals and π-conjugated system and hydroxyl bonds of thymol molecules [43, 45–47].

Figure 7 presents the nitrogen (N_2) adsorption isotherms of hierarchical and thymol-loaded ETS-10 samples. All curves are characteristic of microporous materials, exhibiting Type I isotherm according to the IUPAC classification. As shown in Fig. 7a, the N_2 adsorption capability of ETS-10 samples showed some variation after H_2O_2 treatment. After H_2O_2 treatment, 30-ETS was found to have higher N_2 adsorption capability than ETS. The enhancement of N_2 adsorption capability is associated with enlarged pores in the ETS-10 framework formed after the H_2O_2 treatment. Furthermore, the N_2 adsorption capability of all ETS-10 samples decreased after thymol loading, as shown in Fig. 7b. Thymol molecules fill up the pores, thus preventing N_2 gas adsorption [48]. The lowest N_2 adsorption capability of 30-ETS-thy exhibits the highest thymol loading into the ETS-10 framework.

Table 1 indicates that after the H_2O_2 treatment, the total surface area increased from 328.8 m^2/g to 353.2 and 381.5 m^2/g for 10-ETS and 30-ETS, respectively. A slight increase in the pore volume was also observed from 0.13 cc/g to around 0.15 cc/g upon H_2O_2 treatment. These results show that the H_2O_2 treatment partially removed Ti atoms from the ETS-10 framework. Results further suggest that the partial removal of Ti atoms disrupted the Ti-O-Ti chain creating larger micropores in the framework without significant degradation of crystallinity [29].

The loading of thymol is expected to decrease the surface area and pore volume of ETS-10 crystals. According to Table 1, the total surface area and the pore volume decreased after thymol loading for all ETS-10 samples. A gradual decrease in the total surface area (232.1 m^2/g) and the pore volume (0.09 cc/g) were achieved for 10-ETS-thy. The highest decrease in the surface area and pore volume occurs for

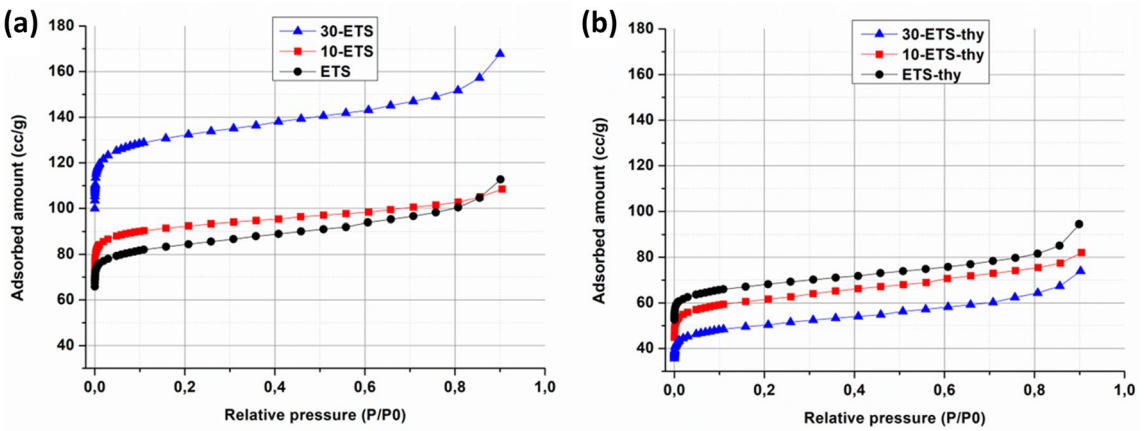


Fig. 7 The N_2 adsorption isotherms of hierarchical and thymol loaded ETS samples

Table 1 BET Surface area, external surface area, micropore surface area and pore volume of ETS-10 samples

Sample Name	S_{total} (m^2/g)[a]	S_{Ext} (m^2/g)[b]	$S_{MicroPore}$ (m^2/g)[b]	Pore volume (cc/g)[c]
ETS	328.8	54.4	274.4	0.13
10-ETS	353.2	34.3	318.9	0.14
30-ETS	381.5	78.8	302.6	0.15
ETS-thy	257.7	42.8	214.9	0.1
10-ETS-thy	232.1	47.1	184.9	0.09
30-ETS-thy	189.4	42.1	147.3	0.08

[a]Determined by multipoint BET

[b]Determined by t-method

[c]Determined by SF method

30-ETS-thy (i.e., 189.4 m^2/g and 0.08 cc/g, respectively), which confer the highest loading compared to 10-ETS-thy and ETS-thy. The thymol loading of the samples was calculated to be 3.14 ± 0.27, 4.51 ± 0.08, and 6.25 ± 0.25 mg/g for ETS-thy, 10-ETS-thy, and 30-ETS-thy, respectively. Accordingly, enlarged micropore size in H_2O_2 treated samples compared to untreated ones correlated with the total amount of thymol loaded in the post-treated samples. In conclusion, the higher thymol loading with enlarged micropore size suggests that the post-treatment of ETS-10 by aqueous H_2O_2 solution is a suitable approach for obtaining more extensive thymol loading in the ETS-10 framework.

3.3 Release assay and kinetics

The in vitro release of thymol at pH 7.0 was examined for as-synthesized and hierarchical ETS-10 crystals (Fig. 8). All release profiles proceeded in two stages; a burst release within the first hour, followed by a slow release observed afterward. Based on the calculated calibration curve of thymol dissolved in PBS, the amount of released thymol was attained for 30-ETS-thy as 42.99 $mg \cdot g^{-1}$. The total amount of released thymol gradually decreased and was estimated to be 28.52 and 15.91 $mg \cdot g^{-1}$ for 10-ETS-thy and ETS-thy, respectively. The complete release was accomplished in 2 days and 16 h for 10-ETS-thy and 1 day and 3 h for ETS-thy. On the other hand, the release process was complete within 4 days and 12 h for 30-ETS-thy. These results indicate that the applied post-treatment influenced the enlargement of the pore structures, causing an extended-release profile. Obtained results correlate with the BET (Table 1) and Raman spectroscopy (Fig. 4) results obtained from post-treated 10-ETS and 30-ETS samples, suggesting increased partial removal of Ti atoms with H_2O_2 treatment amount. For comparison purposes, the thymol encapsulation process was also assessed for mesoporous silica SBA-15. Although the amount loaded was higher than microporous ETS-10 samples, the thymol release from SBA-15 was complete in only 300 min (Supplementary Fig. S2). This result suggests that the post-treatment applied to create defects in the porous network (i.e., 30-ETS-thy) with hierarchical microporosity results in prolonged-release profiles with respect to mesoporous systems (i.e., SBA-15).

Various kinetic models of thymol release from ETS-10 samples were evaluated to fit the experimental data. The calculated release rate (k) for the different models and the coefficient of determination (R^2) are displayed in Table 2. The best-fitting kinetic release profiles of thymol-loaded ETS-10 crystals are illustrated in Fig. 9. The most appropriate model to explain the release mechanism of thymol from untreated ETS-thy was the Higuchi kinetic release model, with the highest R^2 value of 0.9734. The Higuchi kinetic release model is based on Fickian diffusion [49],

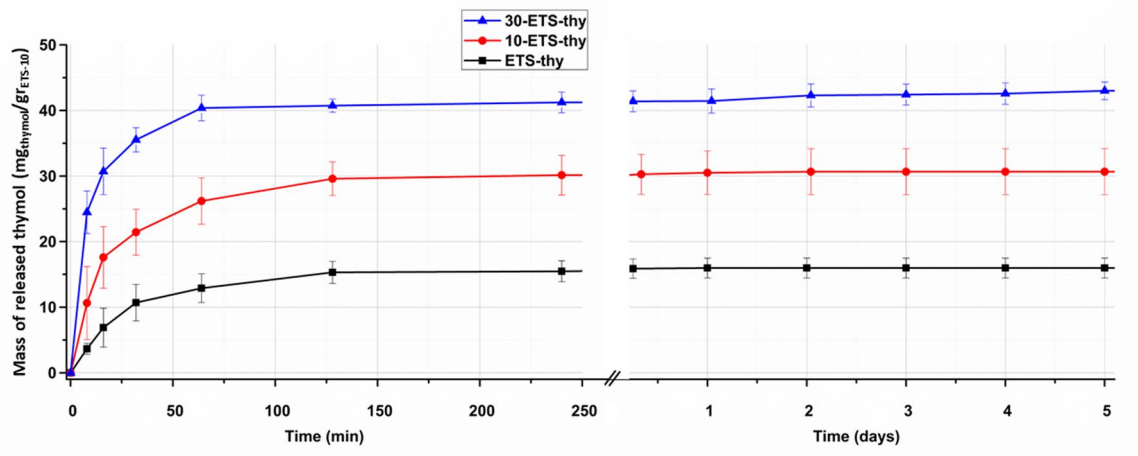


Fig. 8 Release profiles of thymol loaded ETS-10 samples

Table 2 Kinetic release parameters of thymol loaded ETS-10 samples

Release Kinetics Model		ETS-thy	10-ETS-thy	30-ETS-thy
Higuchi	k	10,711	10,893	11,734
$M_t/M_0 = k \times t^{1/2}$	R^2	0,9734	0,9641	0,9174
Korsemeyer-Peppas	k	1,0923	1,0965	1,1167
$M_t/M_0 = k \times t^n$	R^2	0,9393	0,8927	0,8536
Elovich	k	19,806	20,759	22,984
$Q_t = k \times \ln(t)$	R^2	0,9399	0,9888	0,9939
Hixson-Crowell	k	− 0,0065	− 0,0101	− 0,0085
$3\sqrt{Q_0} - 3\sqrt{Q_t} = k \times t$	R^2	0,9375	0,9211	0,8867

indicating that this model is suitable for the systems in which the guest is homogeneously dispersed in the host materials [50].

It was noticeable that the formation of defects into ETS-10 channels produced an alternative release profile to fit the release of thymol from ETS-10 crystals after the H_2O_2 treatment (Table 2). The regression coefficient values (R^2) revealed that the sustained release process of thymol-loaded 10-ETS-thy and 30-ETS-thy conformed to the Elovich model (Fig. 9). Elovich release profile underlines that the thymol release occurs through a logarithmic and time-dependent transport mechanism. In this mechanism, the host's complex framework promotes fast solvent diffusion into and out of the host [25]. The rapid release of adsorbed thymol on the host's outer surface and the slow release of thymol placed in the inner parts of the host was mentioned in this particular release profile [25]. Accordingly, the difference in concentration of H_2O_2 treatment resulted in different pore structures that caused different amounts of thymol loading and release kinetics. These show that the overall structural changes in ETS-10 crystals upon H_2O_2 treatment, i.e., induced disruption in Ti–O–Ti chains resulting in changes in the pore characteristics, affected controllably tailoring the loading and release mechanisms of thymol molecule.

3.4 Antimicrobial assays

The antimicrobial assays of thymol-loaded ETS-10 crystals were assessed against *P. aeruginosa*, *S. aureus*, and *C. albicans* using the disc diffusion method (Fig. 10). The results indicated that all thymol-loaded ETS-10 crystals displayed antimicrobial activity; however, such activity was absent for unloaded ETS-10 crystals (Supplementary Table S1). The inhibition zone diameters are shown in Fig. 10 and listed in Supplementary Table S1. The highest antimicrobial activity was observed against *S. aureus*, with the largest inhibition zones (23 mm) obtained from the 30-ETS-thy sample. A similar but less pronounced trend in enhanced zone inhibition was also observed against *P. aeruginosa* with 30-ETS-thy sample (Supplementary Table S1). The thymol from post-treated ETS-10 samples exhibited weaker antimicrobial activity against *C. albicans* used as yeast, which was not significantly enhanced upon harsher H_2O_2 treatment.

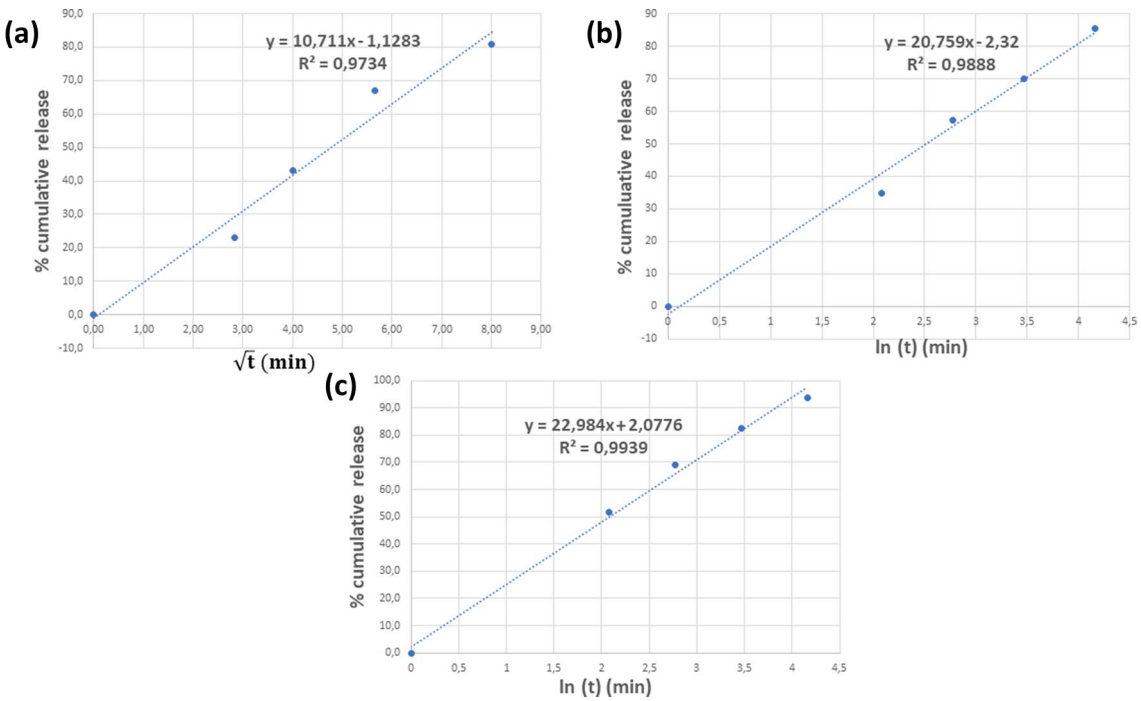


Fig. 9 Higuchi kinetic plots of ETS-thy (**a**) and 10-ETS-thy (**b**). Elovich kinetic plots of 30-ETS-thy (**c**)

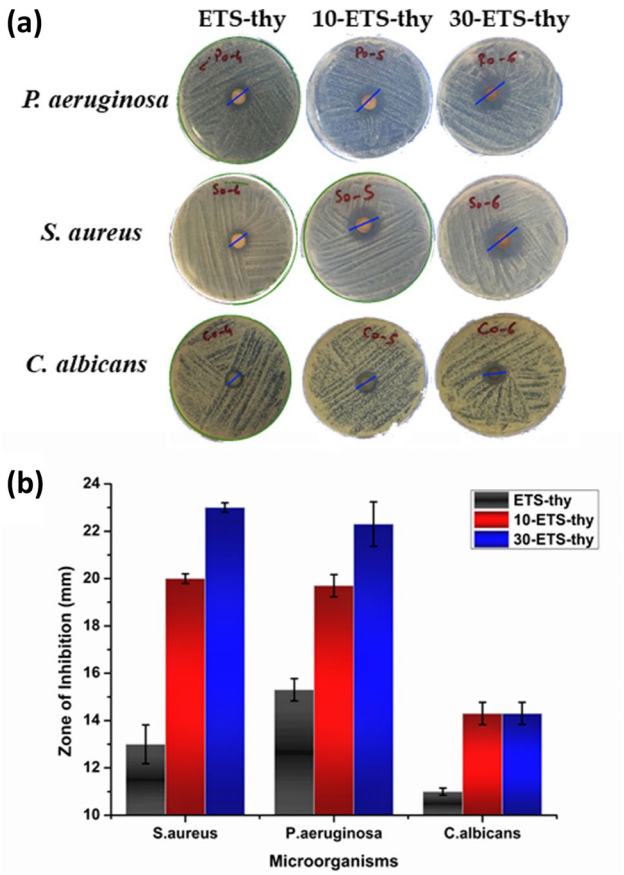


Fig. 10 Inhibition zones of thymol loaded ETS-10 samples against *P. aeruginosa, S. aureus*, and *C. albicans*

Thymol has phenolic structure. Hydroxyl groups in the phenolic structure interrupt the plasma membrane, so the proton motive force (PMF) and electron flow. Hydroxyl constituents also disintegrate the outer membrane of gram-negative bacteria containing lipopolysaccharides and proteins. This disintegration leads to the leakage of lipopolysaccharides. Thymol may also modify the lipid-protein interactions and alter the plasma membrane's protein composition [9, 51, 52]. It is known that phenolic compounds show higher antimicrobial activity against Gram-positive bacteria. Due to the structure of the gram-positive bacterial cell wall, hydrophobic molecules easily penetrate the cells [53]. The outer membrane (OM) found in Gram-negative bacteria distinguishes them from Gram-positive bacteria and makes them more resistant to EOs and other natural extracts with antimicrobial activity. Small soluble hydrophilic molecules can pass through porin proteins located in hydrophilic transmembrane channels, and this is among the reasons why Gram-negative bacteria are relatively resistant to hydrophobic agents [53–55]. Accordingly, increased antimicrobial activity was demonstrated by carefully tailoring ETS-10 pore characteristics using H_2O_2 treatment. These results indicate that creating enlarged micropores is a promising candidate for attaining sustainable antimicrobial solutions for loading essential oil compounds.

4 Conclusion

This study indicates that the hierarchical microporous ETS-10 crystals support a higher amount of thymol encapsulation to allow long-term thymol release and higher antimicrobial activity. The key to this achievement was the improved accessibility of the hierarchical pore system of the ETS-10 framework. The superior accessibility promoted higher encapsulation of thymol in ETS-10 crystals. The H_2O_2 treatment presented a gradual increase in surface area and pore volume of ETS-10 channels. The formation of defects in the ETS-10 framework after the H_2O_2 treatment led to different release profiles of ETS-10 samples, i.e., Higuchi release model for ETS-thy and Elovich release model for 10-ETS-thy and 30-ETS-thy. The thymol release time was prolonged for up to 5 days. All samples exhibited antimicrobial activity against *P. aeruginosa*, *S. aureus*, and *C. albicans*. The antimicrobial activity of thymol-loaded ETS-10 samples increased gradually with an increase in thymol loading. These results indicate that the post-treatment process using H_2O_2 offers an opportunity to enhance antimicrobial activity and extent release profiles for thymol molecules based on altered pore characteristics in microporous systems.

Supplementary Information The online version contains supplementary material available at https://doi.org/10.1007/s10934-022-01367-2.

Acknowledgements No funding was received to assist with the preparation of this manuscript. The support provided by METU-Central Laboratory is greatly acknowledged.

Author contribution All authors contributed to the study conception and design. Material preparation, data collection, and analysis were performed by MIB and DK. The first draft of the manuscript was written by MIB and all authors commented on previous versions of the manuscript. All authors read and approved the final manuscript. Conceptualization: BA, MIB; Investigation: MIB; Resources: BA, DK; Data Curation: MIB; Funding acquisition: BA; Supervision; BA.

Declarations

Conflict of interest The authors declare that they have no known competing financial interests or personal relationships that could have appeared to influence the work reported in this paper.

References

1. B. Prakash, A. Kujur, A. Yadav, A. Kumar, P.P. Singh, N.K. Dubey, Food Control **89**, 1 (2018)
2. A. Jobdeedamrong, R. Jenjob, D. Crespy, Langmuir **34**, 13235 (2018)
3. X. Xu, K. Song, J. Guo, S. Liu, X. Zhou, J. He, J. Porous Mater (2022). https://doi.org/10.1007/s10934-022-01323-0

4. J. Dikić, I. Lukić, J. Pajnik, J. Pavlović, J. Hrenović, N. Rajić, J. Porous Mater. **28**, 1577 (2021)
5. D. Trombetta, F. Castelli, M.G. Sarpietro, V. Venuti, M. Cristani, C. Daniele, A. Saija, G. Mazzanti, G. Bisignano, Antimicrob. Agents Chemother. **49**, 2474 (2005)
6. V.K. Bajpai, A. Sharma, K.H. Baek, Food Control **32**, 582 (2013)
7. F. Bakkali, S. Averbeck, D. Averbeck, M. Idaomar, Food Chem. Toxicol. **46**, 446 (2008)
8. M. Michalska-Sionkowska, M. Walczak, A. Sionkowska, Polym. Test. **63**, 360 (2017)
9. I.M. Helander, H.-L. Alakomi, K. Latva-Kala, T. Mattila-Sandholm, I. Pol, E.J. Smid, L.G.M. Gorris, A. von Wright, J. Agric. Food Chem. **46**, 3590 (1998)
10. M. Karapinar, Ş Esen, Aktuğ, Int. J. Food Microbiol. **4**, 161 (1987)
11. H. Tang, A. Hosein, M. Mattioli-Belmonte, Mater. Sci. Eng. C **120**, 111760 (2021)
12. A. Janatova, A. Bernardos, J. Smid, A. Frankova, M. Lhotka, L. Kourimská, J. Pulkrabek, P. Kloucek, Ind. Crops Prod. **67**, 216 (2015)
13. S. Milovanovic, M. Stamenic, D. Markovic, J. Ivanovic, I. Zizovic, J. Supercrit Fluids **97**, 107 (2015)
14. V.H. Campos-Requena, B.L. Rivas, M.A. Pérez, C.R. Figueroa, E.A. Sanfuentes, LWT - Food Sci. Technol. **64**, 390 (2015)
15. A. Valliammai, A. Selvaraj, P. Mathumitha, C. Aravindraja, S.K. Pandian, Mater. Sci. Eng. C **121**, 111863 (2021)
16. H. Zhong, B. Mu, M. Zhang, A. Hui, Y. Kang, A. Wang, J. Porous Mater. **27**, 843 (2020)
17. F.O.M.S. Abreu, E.F. Oliveira, H.C.B. Paula, R.C.M. De Paula, Carbohydr. Polym. **89**, 1277 (2012)
18. X.H. Chai, R.H. Lin, K.G. Wu, S.R. Li, Adv. Mater. Res. **233–235**, 1766 (2011)
19. A. Rukmani, M. Sundrarajan, J. Ind. Text. **42**, 132 (2011)
20. A. Celebioglu, Z.I. Yildiz, T. Uyar, Food Res. Int. **106**, 280 (2018)
21. G.M. Glenn, A.P. Klamczynski, D.F. Woods, B. Chiou, W.J. Orts, S.H. Imam, J. Agric. Food Chem. **58**, 4180 (2010)
22. B. Niu, Z. Yan, P. Shao, J. Kang, H. Chen, Nanomaterials **8**, 598 (2018)
23. Y. Chen, A. Mensah, Q. Wang, D. Li, Y. Qiu, Q. Wei, Mater. Sci. Eng. C **115**, 111155 (2020)
24. Y. Chen, Y. Qiu, W. Chen, Q. Wei, Mater. Sci. Eng. C **109**, 110536 (2020)
25. B.D. Mattos, B.L. Tardy, M. Pezhman, T. Kämäräinen, M. Linder, W.H. Schreiner, W.L.E. Magalhães, O.J. Rojas, Sci. Rep. **8**, 1 (2018)
26. M. Shahriarinour, F. Divsar, Z. Eskandari, Inorg. Nano-Metal Chem. **49**, 182 (2019)
27. L. Jin, J. Teng, L. Hu, X. Lan, Y. Xu, J. Sheng, Y. Song, M. Wang, J. Sci. Food Agric. **99**, 5168 (2019)
28. L. Rashidi, F. Ganji, F. Dezfoulian, J. Porous Mater. **29**, 1113 (2022)
29. C.C. Pavel, S.H. Park, A. Dreier, B. Tesche, W. Schmidt, Chem. Mater. **18**, 3813 (2006)
30. S. Galioglu, M. Isler, Z. Demircioglu, M. Koc, F. Vocanson, N. Destouches, R. Turan, B. Akata, Microporous Mesoporous Mater. **196**, 136 (2014)
31. H. Rezaeinia, B. Ghorani, B. Emadzadeh, M. Mohebbi, Mater. Sci. Eng. C **115**, 111115 (2020)
32. I.Y. Wu, S. Bala, N. Škalko-Basnet, M.P. di Cagno, Eur. J. Pharm. Sci. **138**, 105026 (2019)
33. F.Q. Pires, J.K.R. da Silva, L.L. Sa-Barreto, T. Gratieri, G.M. Gelfuso, M. Cunha-Filho, Colloids Surf. B Biointerfaces **182**, 110382 (2019)
34. M.W. Anderson, O. Terasaki, T. Ohsuna, P.J.O. Malley, A. Philippou, S.P. Mackay, A. Ferreira, J. Rocha, S. Lidin, Philos. Mag Part. B **71**, 813 (1995)
35. T.K. Das, A.J. Chandwadkar, S. Sivasanker, Bull. Mater. Sci. **17**, 1143 (1994)
36. P.D. Southon, R.F. Howe, Chem. Mater. **14**, 4209 (2002)
37. B. Mihailova, V. Valtchev, S. Mintova, L. Konstantinov, Zeolites **1**(16), 22 (1996)
38. F.X. Llabrés i Xamena, P. Calza, C. Lamberti, C. Prestipino, A. Damin, S. Bordiga, E. Pelizzetti, A. Zecchina, J. Am. Chem. Soc. **125**, 2264 (2003)
39. M.J. Nash, S. Rykov, R.F. Lobo, D.J. Doren, I. Wachs, V. Pennsyl, J. Phys. Chem. C **111**, 7029 (2007)
40. D.R.C. Huybrechts, I. Vaesen, H.X. Li, P.A. Jacobs, Catal Lett. **8**, 237 (1991)
41. W. Lin, H. Frei, J. Am. Chem. Soc. **124**(31), 9292 (2002)
42. P. Ratnasamy, D. Srinivas, Adv. Catal. **48**, 1 (2004)
43. A. Zecchina, F.X. Llabrés i Xamena, C. Pazè, G. Turnes Palomino, S. Bordiga, C. Otena, Areán, Phys. Chem. Chem. Phys. **3**, 1228 (2001)
44. S. Kim, W. Choi, J. Phys. Chem. B **109**, 5143 (2005)
45. F. Geobaldo, S. Bordiga, A. Zecchina, E. Giamello, G. Leofanti, G. Petrini, Cat. Lett. **16**, 109 (1992)
46. S. Bordiga, G. Ricchiardi, G. Spoto, D. Scarano, L. Carnelli, A. Zecchina, C.O. Areán, J. Chem. Soc. Faraday Trans. **89**, 1843 (1993)
47. U. Wilkenhöner, E. van Steen, G. Langhendries, G.V. Baron, F. van Laar, P.A. Jacobs, D.W. Gammon, J. Catal. **203**, 201 (2001)
48. A. Bernardos, T. Marina, P. Žáček, É Pérez-Esteve, R. Martínez-Mañez, M. Lhotka, L. Kouřimská, J. Pulkrábek, P. Klouček, J. Sci. Food Agric. **95**, 2824 (2015)
49. M.P. Paarakh, P.A.N.I. Jose, C.M. Setty, G.V. Peter, Int. J. Pharm. Res. Technol. **8**, 12 (2019)
50. D. Tan, P. Yuan, F. Annabi-Bergaya, D. Liu, L. Wang, H. Liu, H. He, Appl. Clay Sci. **96**, 50 (2014)
51. A. Gafur, G.Y. Sukamdani, N. Kristi, A. Maruf, J. Xu, X. Chen, G. Wang, Z. Ye, J. Mater. Chem. B **8**, 9825 (2020)
52. A. Ultee, M.H.J. Bennik, R. Moezelaar, Appl. Environ. Microbiol. **68**, 1561 (2002)
53. F. Nazzaro, F. Fratianni, L. de Martino, R. Coppola, V. de Feo, Pharmaceuticals **6**, 1451 (2013)
54. M. Vaara, Microbiol. Rev. **56**, 395 (1992)
55. H. Nikaido, Science **264**, 382 (1994)

Publisher's Note Springer Nature remains neutral with regard to jurisdictional claims in published maps and institutional affiliations.

Springer Nature or its licensor (e.g. a society or other partner) holds exclusive rights to this article under a publishing agreement with the author(s) or other rightsholder(s); author self-archiving of the accepted manuscript version of this article is solely governed by the terms of such publishing agreement and applicable law.